



Article

Interplay Between Atmospheric Correction and Fusion Techniques Enhances the Quality of Remote Sensing Image Fusion

Yang Li ^{1,2,3} , Feinan Chen ^{1,3} , Tangyu Sui ^{1,2,3}, Rufang Ti ^{1,3}, Weihua Cheng ^{1,3}, Jin Hong ^{1,3} and Zhenwei Qiu ^{1,3,*}

¹ Hefei Institutes of Physical Science, Chinese Academy of Sciences, Hefei 230031, China; hiliyang@mail.ustc.edu.cn (Y.L.)

² Graduate School of Science Island, University of Science and Technology of China, Hefei 230026, China

³ Key Laboratory of Optical Calibration and Characterization, Chinese Academy of Sciences, Hefei 230031, China

* Correspondence: zwqiu@aiofm.ac.cn; Tel.: +86-13716526194

Abstract: Remote sensing image fusion technology integrates observational data from multiple satellite platforms to leverage the complementary advantages of the different types of remote sensing images. High-quality fused remote sensing images provide detailed information on surface radiation, climate, and environmental conditions, thereby supporting governmental policies on environmental changes. Improving the quality and quantitative accuracy of fused images is a crucial trend in remote sensing image fusion research. This study investigates the impact of atmospheric correction and five widely applied fusion techniques on remote sensing image fusion. By constructing four fusion frameworks, it evaluates how the choice of fusion method, the implementation of atmospheric correction, the synchronization of atmospheric parameters, and the timing of atmospheric correction influence the outcomes of remote sensing image fusion. Aerial flights using remote sensors were conducted to acquire atmospheric parameter distribution images that are strictly synchronous with the remote sensing images. Comprehensive and systematic evaluations of the fused remote sensing images were performed. Experiments show that for the remote sensing images used, selecting the appropriate fusion method can improve the spatial detail evaluation metrics of the fused images by up to 2.739 times, with the smallest deviation from true reflectance reaching 35.02%. Incorporating synchronous atmospheric parameter distribution images can enhance the spatial detail evaluation metrics by up to 2.03 times, with the smallest deviation from true reflectance reaching 5.4%. This indicates that choosing an appropriate fusion method and performing imaging-based synchronous atmospheric correction before fusion can maximize the enhancement of spatial details and spectral quantification in fused images.

Keywords: remote sensing; synchronous atmospheric correction; image fusion; quality evaluation; quantification



Citation: Li, Y.; Chen, F.; Sui, T.; Ti, R.; Cheng, W.; Hong, J.; Qiu, Z. Interplay Between Atmospheric Correction and Fusion Techniques Enhances the Quality of Remote Sensing Image Fusion. *Remote Sens.* **2024**, *16*, 3916. <https://doi.org/10.3390/rs16213916>

Academic Editors: Qian Du, Jun Zhou, Danfeng Hong and Chenhong Sui

Received: 28 August 2024

Revised: 9 October 2024

Accepted: 11 October 2024

Published: 22 October 2024



Copyright: © 2024 by the authors. Licensee MDPI, Basel, Switzerland. This article is an open access article distributed under the terms and conditions of the Creative Commons Attribution (CC BY) license (<https://creativecommons.org/licenses/by/4.0/>).

1. Introduction

Advancements in space technology have significantly increased both the diversity and quantity of remote sensors, resulting in an abundant array of remote sensing image resources [1]. Achieving both a multispectral and a wide instantaneous field of view in remote sensing images is challenging while maintaining a high signal-to-noise ratio. This limitation implies that a single remote sensor often cannot simultaneously capture images with both high spatial resolution and multispectral resolution [2]. Remote sensing image fusion technology integrates images with different spatial and spectral resolutions to produce a composite image that combines both high spatial and multispectral resolution. This technique enables the fused image to present detailed information with enhanced

spatial clarity and spectral richness [3]. High-quality, quantitative remote sensing image fusion must not only achieve high spatial and multispectral resolution but also ensure accurate spectral quantification. This means that the pixel values must be computable to derive physical information about the Earth's surface, such as radiance or reflectance, within the response wavelength range of the sensor. Quantitative fusion of panchromatic and multispectral color remote sensing images have widespread applications, offering reliable foundations for research in areas such as land cover change [4], terrestrial ecosystem monitoring [5], and the monitoring and classification of forests and crops [6,7]. Additionally, government agencies can leverage these high-quality fused images to develop policies that address environmental changes and ensure the sustainable management of land resources [8].

To achieve the quantitative fusion of remote sensing images, researchers have undertaken significant efforts. For example, in 2011 [9], an improved additive wavelet transform was introduced for fusion, capable of preserving both radiometric and geometric information. In 2012 [10], a multisensor image fusion method based on a hidden Markov tree and a pulse-coupled neural network (PCNN) was proposed. This method uses a PCNN to select the maximum value for low-pass coefficients and a saliency-based rule for directional coefficients, addressing minor distortions in structural components. In 2013 [11], the authors proposed a fusion method based on variational wavelets, which perform well with highly heterogeneous data. In 2014 [12], the authors explored contourlet representation and introduced an adjustable contourlet transform for effective fusion, averaging the low-pass coefficients and selecting the absolute maximum value for directional coefficients. This method corrects minor structural distortions and radiometric blurring. In 2015 [13], a region division strategy was used in the shearlet domain for pansharpening, applying region-correlation-based fusion rules to all decomposed coefficients. Significant spatial enhancement was observed as a result of these region-based rules. In 2016 [14], a pansharpening method in the shearlet domain was proposed, considering regional correlation metrics and applying local-region-based fusion rules to approximation coefficients and gradient-based fusion rules to directional coefficients. The results demonstrate that this method effectively preserves structural and radiometric information. In 2018, [15] conducted the spatiotemporal fusion study using deep convolutional neural networks (CNNs) in the context of massive remote sensing data. In 2019, [16] presented a region-based fusion scheme for combining panchromatic, multispectral, and synthetic aperture radar images. Temporal data fusion and high spatial methods were used to generate synthetic Landsat imagery by combining Landsat and MODIS data. In 2021 [17], a new region-based fusion method combining non-subsampled contourlet transform (NSCT) and particle swarm optimization (PSO) was proposed. This method applies a maximum-based rule to the approximation layer, separates band-pass coefficients into smooth regions, and uses PSO for edge regions and a maximum-based rule for separated components. It performs well in spatial enhancement and mitigates minor blurring effects.

In recent years, deep-learning-based fusion methods have been categorized into three types based on the supervisory paradigms employed during the training process: unsupervised, self-supervised, and supervised approaches [18]. Supervised methods utilize ground truth values to guide the training processes, while unsupervised approaches construct loss functions by constraining the similarity between the fusion results and the source images. Self-supervised algorithms are commonly associated with the AutoEncoder (AE)-based framework. In 2020, [19] introduced the pansharpening generative adversarial network (Pan-GAN), the first method to explore the unsupervised fusion of multispectral and panchromatic images. This approach incorporates two discriminators that create adversarial relationships between the fusion result and the two source images, each assessing the fidelity of spectral and spatial information, respectively. Ref. [20] introduced a semantic-aware real-time image fusion network (SeAFusion) in the same year. This study employs a cascading approach that integrates a fusion module with a semantic segmentation module, allowing semantic loss to guide high-level semantic information

to flow back to the fusion module. Additionally, it proposes methods such as gradient residual dense block (GRDB) to bridge the gap between image fusion and high-level vision tasks. The concept of self-supervised edge-attention guidance for image fusion (EAGIF) was proposed in [21], utilizing a coarse-to-fine deep architecture to learn multiscale features from multimodal images. It also designs an edge-guided attention mechanism based on these multiscale features to focus the fusion process on common structures, thereby enhancing detail recovery while attenuating noise. Supervised fusion methods, as proposed in [22–25], illustrate the advancements that deep learning has contributed to image fusion techniques. In 2017, [22] proposed the pansharpening deep network architecture (PanNet), which employs residual learning to shift network training to the high-frequency domain. This approach allows the network to focus on learning high-frequency structural information, thereby enhancing the spatial quality of the fusion results. Ref. [23] proposed the super-resolution-guided progressive pansharpening neural network (SRPPNN), which incorporates two specific structural designs: a super-resolution module and progressive learning. These features enable the network to continuously capture spatial details at various scales and progressively integrate them into the upsampled multispectral images. Ref. [24] proposed the gradient projection-based pansharpening neural network (GPPNN), which investigates generative models for panchromatic and multispectral images. This approach explores the spatial and spectral degradation processes and uses them as priors to guide the optimization of neural networks, thereby enhancing fusion performance. In 2022, [25] introduced GTP-PNet, which employs a specialized transformation network (TNet) to model the spectral degradation process. This method establishes a more accurate nonlinear regression relationship between multispectral and panchromatic images in the gradient domain. The nonlinear regression relationship is used as a prior to constrain the preservation of spatial structures, thereby ensuring a balance between spectral and spatial information.

The research discussed above primarily focuses on improving fusion results through various approaches, including advancements in image decomposition methods [9,11,12,14], the establishment of stringent criteria for selecting fusion coefficients [10,13,17], enhancing the accuracy of nonlinear spectral fitting [22,25], and optimizing detail and spectral quantitative guidance [19–21,23,24]. However, there are still some problems in quantitative remote sensing image fusion. The information in remote sensing images represents a combination of atmospheric and surface data. Atmospheric effects not only reduce contrast and blur detail textures in panchromatic images [1], but also distort spectral information and decrease the quantitative accuracy of multispectral color images [26]. As a result, the fused images obtained under these conditions exhibit blurred spatial details and errors in color spectral information, failing to meet the requirements for quantitative remote sensing image fusion. Most research considers atmospheric information as part of remote sensing image data and employs mathematical methods to develop updated and more efficient fusion algorithms. However, the impact of atmospheric effects is often overlooked. This neglect prevents significant improvements in the spatial detail and spectral quantification of fused images. Additionally, aerosol observation methods are relatively limited, and aerosols exhibit strong spatiotemporal heterogeneity [27]. This results in aerosol parameters that often do not align temporally and spatially with the remote sensing images, leading to residuals in atmospheric correction results [28].

The primary objective of this study is to explore methods for obtaining highly synchronous aerosol optical depth (AOD) and column water vapor (CWV) measurements and integrating these atmospheric parameters as source images for fusion with panchromatic and multispectral remote sensing images. This approach aims to mitigate the impact of atmospheric effects on the quantitative fusion of remote sensing images. The study examines the interaction between atmospheric correction and five widely used fusion methods: principal component analysis (PCA) [3], intensity-hue-saturation (IHS) [29], Laplacian pyramid (LP) [30], discrete wavelet transform (DWT) [4], and non-subsampled contourlet transform (NSCT) [31]. It investigates how factors such as the choice of fusion methods,

atmospheric correction, the synchronization of atmospheric parameters, and the timing of atmospheric correction affect the quality of fused remote sensing images. The findings provide a valuable reference for establishing robust quantitative fusion processes. The data for this study were obtained from airborne flight experiments involving multiple remote sensors, enabling a systematic comparison of spatial detail and spectral quantitative accuracy in the fused images.

2. Materials and Methods

2.1. Image Fusion

This study employed five classic and widely used pixel-level remote sensing image fusion techniques, including the IHS and PCA fusion methods based on spatial domain techniques, as well as the LP, DWT, and NSCT fusion methods based on transform domain techniques. To ensure that the fused images achieved spectral quantitative accuracy and spatial resolution, and to enhance the comparability of different fusion methods, the fusion rules should ideally extract spatial details from the panchromatic images while deriving spectral information from the multispectral images [3].

2.1.1. Spatial-Domain-Based Image Fusion

The spatial domain techniques were based on the projection of a multispectral image into another space using a transformation that separates the spatial structure from the spectral information in different components. Then, the component containing the spatial structure was replaced with the panchromatic image. A greater correlation between the replaced component and the panchromatic image produces less distortion [32].

IHS and PCA are two commonly used spatial domain methods for image fusion. PCA-based image fusion calculates and combines the principal components of the original images to reduce data dimensionality and extract image information. While PCA effectively preserves the overall information of the image, it may lead to color distortion. In contrast, the IHS transformation decomposes a color image into three components: intensity, hue, and saturation, and performs fusion on the intensity component. The IHS method is effective in preserving color information but is prone to a loss of image details.

The fusion rules for the IHS and PCA methods follow the principle of component substitution, as illustrated in Figure 1; Image_P represents the panchromatic image, while Image_M denotes the multispectral image. The specific steps for fusion are as follows: (1) Perform PCA/IHS transformation on the R, G, and B bands of the multispectral image. (2) Conduct histogram matching between the first principal component or intensity component obtained from the PCA/IHS transformation and the panchromatic image, replacing the first principal component or intensity component with the histogram-matched panchromatic image. (3) Finally, apply the inverse PCA/IHS transformation to generate the fused image, designated as Image_F.

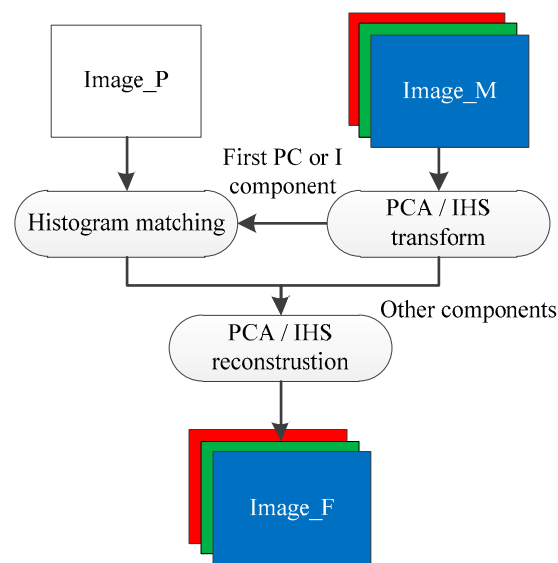


Figure 1. Fusion diagram based on IHS and PCA methods.

2.1.2. Transform-Domain-Based Image Fusion

Transform domain fusion methods involve the multiscale decomposition of images, generating low-frequency subband coefficients that contain most of the spectral information and high-frequency subband coefficients that capture most of the spatial details. LP, DWT, and NSCT are three classical transform domain fusion methods, with their primary difference lying in the level of image decomposition. The LP fusion method is relatively simple, employing Gaussian pyramid decomposition to express images at multiple scales and resolutions. However, LP exhibits insufficient directional decomposition and is prone to matrix artifacts. The DWT fusion method decomposes images into different scales and resolutions using two-dimensional separable discrete wavelets, offering good time-frequency analysis capabilities; however, DWT representation is not sparse. In contrast, NSCT iteratively decomposes images using the non-subsampled Laplacian pyramid (NSP) to generate images at various scales, followed by further multidirectional decomposition through the non-subsampled directional filter bank (NSDFB). As a result, NSCT provides image decomposition with multiscale, multidirectional, and translation-invariant properties.

Although the three fusion methods differ in their approaches and levels of image decomposition, the resulting subband coefficients can all be categorized into high-frequency and low-frequency. To ensure the comparability of the fused images, the multiscale decomposition level was uniformly set to three, meaning that the image underwent three iterations of scale decomposition. For low-frequency, the fusion rule involved retaining the low-frequency subband coefficients of the decomposed multispectral image. For high-frequency, to avoid artifacts and ensure a smooth transition between spatial details and spectral information, a fusion rule based on a matching degree was applied [33]. This rule was determined by the salience and matching degree of the high-frequency subband coefficients.

Figure 2 illustrates the fusion processes for the LP, DWT, and NSCT methods. The specific steps for fusion are as follows: (1) Perform LP/DWT/NSCT decomposition on the panchromatic and multispectral color images to obtain the subband coefficients for each image, with the R, G, and B channels of the multispectral color image decomposed separately. (2) Apply a matching degree-based fusion rule to combine the high-frequency subband coefficients that share the same decomposition scale and direction, resulting in the high-frequency subband coefficients of the fused image. The low-frequency subband coefficients from the color image are retained as the low-frequency subband coefficients of the fused image. (3) Reconstruct the fused high-frequency and low-frequency subband coefficients and perform the inverse LP/DWT/NSCT transformation to obtain the fused image, designated as Image_F.

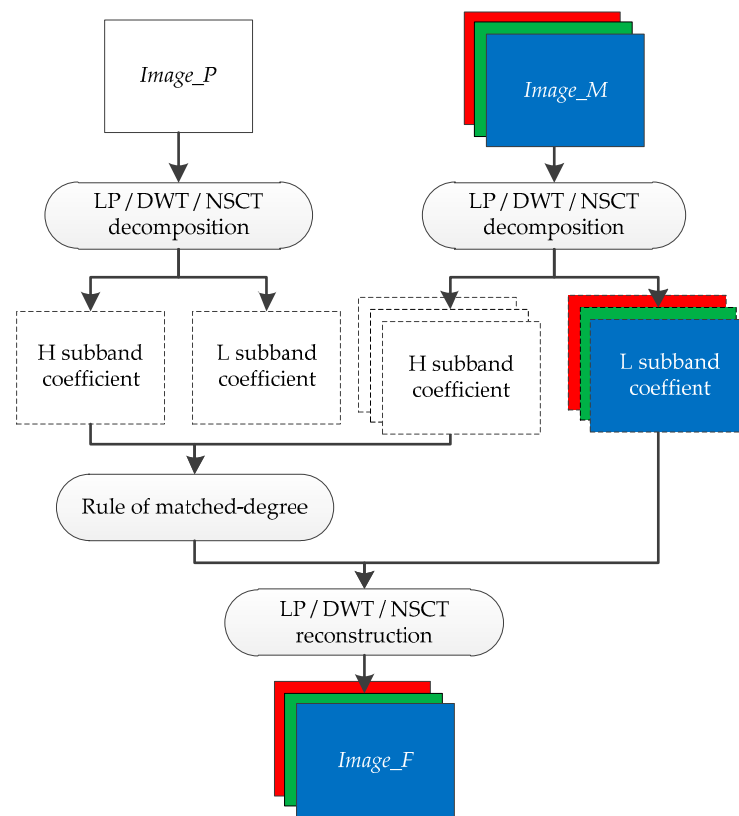


Figure 2. Fusion diagram based on LP, DWT, and NSCT methods.

2.1.3. Fusion of Images and Atmospheric Parameters

The purpose of fusing atmospheric parameters (AOD and CWV) with panchromatic and multispectral remote sensing images was to perform atmospheric correction, thereby mitigating or even eliminating atmospheric effects. The fusion rules were determined by the 6S atmospheric radiative transfer model [34,35], which establishes a representation of visible and near-infrared band reflectance in relation to the ground bidirectional reflectance distribution function (BRDF) at the top of the atmosphere, as shown in Equations (1) and (2):

$$\rho_{TOA} = \rho_0 + T_g \left[AB\rho_S + AC\bar{\rho} + AD\bar{\rho}' + CD\bar{\bar{\rho}} + \frac{(B+C)(A+D)S(\bar{\rho})^2}{1 - S\bar{\rho}} \right] \quad (1)$$

$$A = e^{-\tau/\mu_V}, \quad B = e^{-\tau/\mu_S}, \quad C = t_d(\mu_S), \quad D = t_d(\mu_V) \quad (2)$$

where the variable ρ_{TOA} represents the reflectance observed at the top of the atmosphere. ρ_0 denotes the atmospheric path radiance reflectance, while ρ_S represents the surface target reflectance. S is the hemisphere reflectance in the downward direction of the lower atmosphere. μ_S corresponds to the cosine of the solar zenith angle, and μ_V is the cosine of the satellite zenith angle. The terms B and C signify the atmospheric transmittance for direct solar radiation and atmospheric diffuse radiation reaching the ground, respectively. Similarly, A and D represent the atmospheric transmittance for the direct reflectance from the ground to the sensor and the atmospheric transmittance for the diffuse radiation reaching the sensor from the ground. τ represents the atmospheric optical thickness. Additionally, $\bar{\rho}$, $\bar{\rho}'$, and $\bar{\bar{\rho}}$ stand for the hemisphere reflectance scattered by the atmosphere to the ground, the ground hemisphere reflectance scattered back into the atmosphere, and the ground hemisphere reflectance after two scattering events through both the atmosphere and the ground, respectively. These variables are dependent on atmospheric optical parameters and surface reflection characteristics. T_g represents the absorption by atmospheric components such as ozone and water vapor in the visible and near-infrared spectra. It is evident that to

determine the ground reflectance ρ_s , a series of intermediate parameters must be obtained. Among these, A, B, C, D, S, T_g , and ρ_0 are solely related to atmospheric conditions and are calculated by the 6S model based on AOD and CWV. $\bar{\rho}, \bar{\rho}'$, and $\bar{\rho}$ are related to image pixels and are determined by the 6S model using the BRDF model.

To facilitate the rapid fusion of atmospheric parameter distribution images with remote sensing images, an atmospheric correction lookup table (LUT) was established [36]. The principle of the LUT is to pre-compute and store the results of radiative transfer models under various conditions, enabling quick lookup and application during actual processing. The parameters setting of 6S model are shown in the Table 1. A range of values was defined for observation geometry, AOD, and CWV, with step values set to iterate through the specified parameter values. The 6S model was then run iteratively, traversing through predefined parameter settings to generate a lookup table for parameters a, b, and c. The relationship between image pixel values before and after atmospheric correction can be expressed using a computational formula based on these parameters, as shown in Equation (3):

$$output = \frac{a \times input - b}{1 + (a \times input - b) \times c} \quad (3)$$

Table 1. Set the 6S model parameters to establish the LUT.

Name	Setting Parameter Values
Molecular atmosphere model	Mid latitude winter
Aerosol model	Continental
Surface reflectance	BRDF
Response band	Spectral response of main cameras
Observation geometry	In dataset
AOD at 550 nm	Range of 0.20 to 0.80, with a step increment of 0.001.
CWV (g/cm ³)	Range of 0.80 to 1.80, with a step increment of 0.01.

The fusion process of atmospheric parameters (AOD and CWV) with the remote sensing image can be illustrated as shown in Figure 3. For each pixel, the corresponding AOD and CWV indices are used to extract the three parameters from the lookup table for fusion calculations, where \otimes represents Equation (5). The values in the fused image represent the reflectance with atmospheric effects removed or minimized (which can also be expressed in terms of radiance). The accuracy and precision of the atmospheric parameters AOD and CWV determine the spatial detail clarity and spectral quantification of the fused remote sensing image.

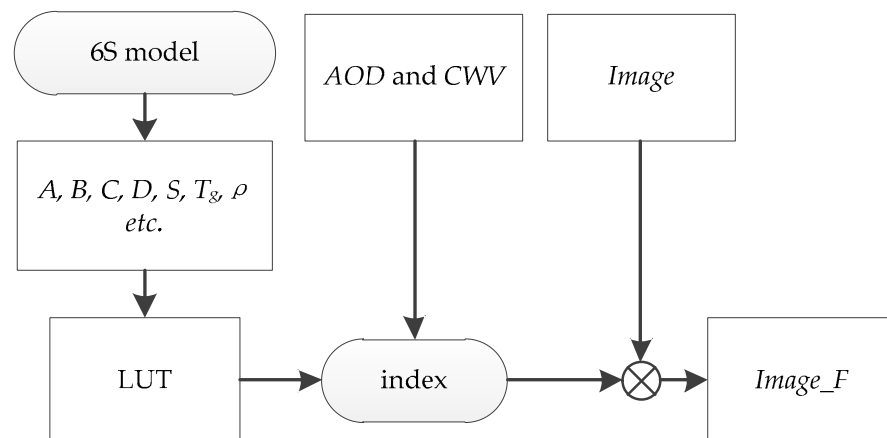


Figure 3. Atmospheric parameters and remote sensing image fusion.

2.2. Evaluation Metrics

This study categorized the widely used quality evaluation metrics for remote sensing image fusion into three types based on factors such as calculation methods and their physical significance:

- Spectral domain: The evaluation metrics in the spectral domain are used to reflect the degree of spectral variation or distortion in the images. This can be represented by comparing the reflectance calculated from the image with the actual reflectance measured through experimental means, namely the deviation from true reflectance (DTR).
- Spatial domain: The evaluation metrics in the spatial domain assess spatial details such as edges and textures within the image. These can be represented through structural and feature-based measures, including the average gradient (AG) [17], standard deviation (SD) [37], normalized correlation coefficient (NCC) [38], Structural SIMilarity (SSIM) [38], and universal image quality index (UIQI) [39].
- Informational domain: The evaluation metrics in the information domain are used to infer the amount of information contained in the images. This can be expressed through statistical indicators of the images and relevant measures from information theory, such as the normalized mutual information (NMI) [40] and information entropy (EN) [37].

Next, the calculation methods and significance of each evaluation metric will be introduced. Table 2 presents the attributes of these evaluation metrics.

Table 2. Attributes of the evaluation metrics.

Name	Classification	Meaning	Number of Images Required
AG	Spatial	Contrast and texture	1
SD	Spatial	Dispersion	1
EN	Informational	Information content	1
NCC	Spatial	Correlation	2
SSIM	Spatial	Structural similarity	2
NMI	Informational	Information similarity	2
UIQI	Spatial	Structural similarity	3
DTR	Spectral	Spectral quantification	1

1. Average Gradient

The definition formula of *AG* is shown in Equation (4), where *F* represents the fused image, and the dimensions of the image are $M \times N$. Generally, a higher average gradient in the fused image indicates greater contrast, which is typically associated with better fusion quality.

$$AG = \frac{1}{(M-1)(N-1)} \sum_{i=1}^{M-1} \sum_{j=1}^{N-1} \sqrt{\frac{[F(i+1,j) - F(i,j)]^2 + [F(i,j+1) - F(i,j)]^2}{2}} \quad (4)$$

2. Standard Deviation

The calculation formula of *SD* is shown in Equation (5), where \bar{F} represents the mean gray value of the fused image. A larger *SD* in the fused image suggests a more dispersed distribution of gray levels, which is generally considered indicative of better image quality.

$$SD = \sqrt{\frac{1}{M \times N} \sum_{i=1}^{M-1} \sum_{j=1}^{N-1} [F(i,j) - \bar{F}]^2} \quad (5)$$

3. Entropy

The calculation formula of EN is shown in Equation (6), where p represents the gray level distribution of the fused image, n is the dynamic range of the pixels, and p_i is the probability of a pixel in the fused image having a gray level of i . A higher EN in the fused image indicates a greater amount of information contained within it, which is generally regarded as a sign of better image quality.

$$EN = -\sum_{i=1}^n p_i \log_2 p_i \quad (6)$$

4. Normalized Correlation Coefficient

The definition of NCC is given by Equation (7), where R represents the image before fusion and \bar{R} represents the mean value. The NCC compares the two images before and after fusion; a higher NCC value indicates a greater correlation between the two images.

$$NCC = \frac{\sum_{i=1}^M \sum_{j=1}^N [(R(i,j) - \bar{R})(F(i,j) - \bar{F})]}{\sqrt{\sum_{i=1}^M \sum_{j=1}^N (R(i,j) - \bar{R})^2 \sum_{i=1}^M \sum_{j=1}^N (F(i,j) - \bar{F})^2}} \quad (7)$$

5. Structural Similarity

The $SSIM$ evaluates image performance by comparing differences in brightness, contrast, and texture distortion between images. The comparison functions for brightness, contrast, and structure are presented in Equation (8). Constants C_1 , C_2 , and C_3 in Equation (9) are introduced to ensure stability when the denominator approaches zero, and are related to the dynamic range of the remote sensing image pixels, n . The standard deviations of the image before fusion and the fused image are denoted as σ_R and σ_F , respectively, while σ_{RF} represents the covariance between the image before fusion and the fused image.

$$l(R, F) = \frac{2\bar{R}\bar{F} + C_1}{\bar{R}^2 + \bar{F}^2 + C_1}, \quad c(R, F) = \frac{2\sigma_R\sigma_F + C_2}{\sigma_R^2 + \sigma_F^2 + C_2}, \quad s(R, F) = \frac{2\sigma_{RF} + C_3}{\sigma_R\sigma_F + C_3} \quad (8)$$

$$C_1 = (0.01 \times n)^2, \quad C_2 = (0.03 \times n)^2, \quad C_3 = \frac{C_2}{2} \quad (9)$$

Combining Equations (8) and (9), the $SSIM$ function can be derived as shown in Equation (10):

$$SSIM(R, F) = [l(R, F)]^\alpha [c(R, F)]^\beta [s(R, F)]^\gamma \quad (10)$$

α , β , and γ represent the relative importance of each metric and sum to 1. The $SSIM$ compares the two images before and after fusion; a higher $SSIM$ value indicates greater structural similarity between the two images.

6. Normalized Mutual Information

The definition of MI is given by Equation (11), where q represents the distribution of the image before fusion R , and q_i denotes the probability that a pixel in R has a grayscale value of i . Additionally, $\gamma_{i,j}$ represents the joint probability density of R and F .

$$MI = \sum_{i=1}^n \sum_{j=1}^n \gamma_{i,j} \log_2 \frac{\gamma_{i,j}}{p_i q_i} \quad (11)$$

The normalization method of *MI* is detailed in Equation (12). It compares the two images before and after fusion; a higher *NMI* value indicates a greater degree of dependence between the two images.

$$NMI(R, F) = \frac{2MI(R, F)}{-\sum_{i=1}^n p_i \log_2 p_i - \sum_{j=1}^n q_j \log_2 q_j} \quad (12)$$

7. Universal Image Quality Index

Similar to the *SSIM*, the *UIQI* also consists of three components that reflect the loss of correlation between signals, luminance distortion, and contrast distortion. The *UIQI* between the two images is represented by Equation (13):

$$UIQI(R, F) = \frac{2\sigma_{RF}\overline{RF}}{(\sigma_R^2 + \sigma_F^2)(\overline{R}^2 + \overline{F}^2)} \quad (13)$$

By conducting a region-based evaluation of the image, the formula can be expressed as Equation (14):

$$UIQI(R, F) = \frac{1}{|W|} \sum UIQI(R, F|w) \quad (14)$$

where W represents the sum of all windows, $|W|$ denotes the cardinality of W , and $UIQI(R, F|w)$ indicates the similarity between images R and F within window w , as calculated by Equation (13). Next, by introducing the two images prior to fusion, we calculate the overall similarity between the fused image F and the images P and R before fusion, as shown in Equation (15):

$$UIQI(P, R, F) = \frac{1}{|W|} \sum_{w \in W} [\lambda(w)UIQI(P, F|w) + (1 - \lambda(w))UIQI(R, F|w)] \quad (15)$$

where the formula for calculating the weight $\lambda(w)$ is given in Equation (16):

$$\lambda(w) = \frac{s(P|w)}{s(P|w) + s(R|w)} \quad (16)$$

and s represents the saliency measure of the image within the window, which in this paper, is expressed by the image's contrast. *UIQI* compares the three images before and after fusion; a higher value indicates a greater overall similarity between the fused image and the two images prior to fusion.

8. Deviation from True Reflectance

Define *DTR* as the percentage difference between the true surface reflectance and the reflectance calculated from the image, as shown in Equation (17):

$$\eta(R_{surface}, F) = \frac{\left| \frac{1}{MN} \sum_{i=1, j=1}^{M, N} F(i, j) - R_{surface} \right|}{R_{surface}} \times 100\% \quad (17)$$

Here, $R_{surface}$ represents the measured reflectance at the surface, and (i, j) indicates the coordinates of the target in the remote sensing image. This study uses the measurements obtained from the ground-based Analytical Spectral Devices (ASDs) as the true reflectance.

2.3. Data

The aerial flight experiments were conducted to acquire remote sensing images. The instruments utilized in these experiments included the visible near infrared airborne synchronous monitoring atmospheric corrector (VNIR-ASMACH), the short wave infrared

ASMAC (SWIR-ASMAC), a high-resolution panchromatic camera, a multispectral color camera, a gyroscope, GPS, the CE318 sun photometer, and ASDs. To achieve synchronous imaging across the various remote sensors, the pulse signals generated during imaging by VNIR-ASMAC and SWIR-ASMAC served as the reference. These signals were subsequently transmitted through hardware to trigger imaging in both the high-resolution panchromatic camera and the multispectral color camera. Figure 4 illustrates some of the images obtained during the aerial flight experiments.

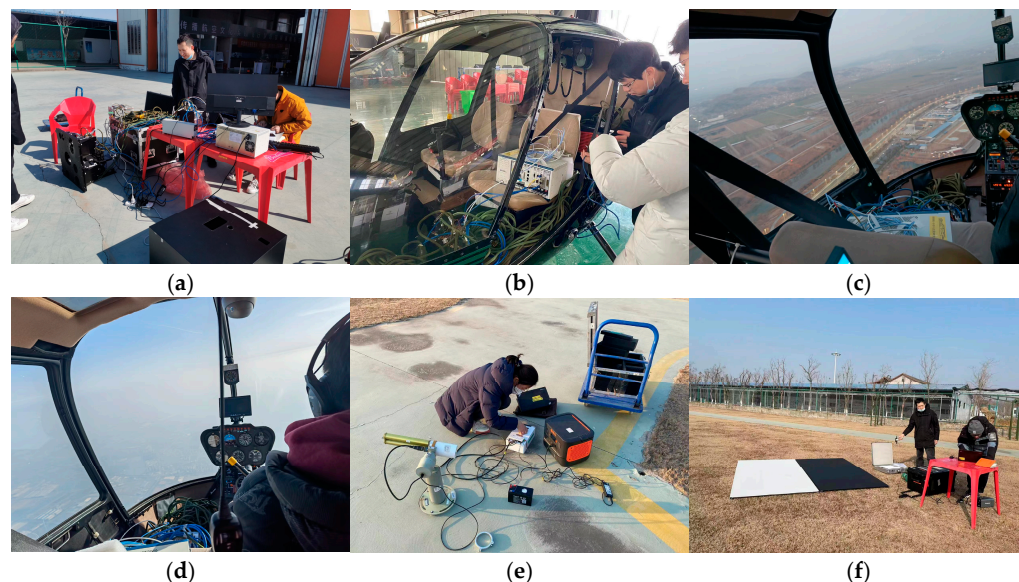


Figure 4. Aerial flight experiments: (a) ground operation; (b) in-helicopter testing; (c) low-altitude aerial experiment; (d) high-altitude aerial experiment; (e) data collection by CE318; (f) data collection by ASDs.

2.3.1. Panchromatic and Multispectral Color Remote Sensing Images

The main cameras used in this experiment were the panchromatic camera, model LBAS-U350-74M, and the multispectral color camera, model LBAS-U350-74C, both manufactured by LUSTER. The main distinction between the two cameras lies in the color camera's incorporation of the Bayer filter, which enables the acquisition images of the R, G, and B band. Figure 5a,b provides physical diagrams of the cameras. Both cameras underwent geometric calibration, radiometric calibration, and spectral response testing, enabling the conversion of the digital number (DN) values of remote sensing images into radiance values corresponding to their respective wavelengths.

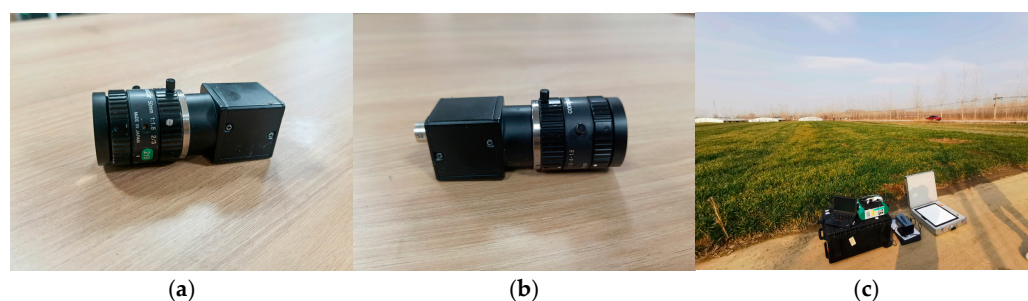


Figure 5. Main cameras devices on the ground: (a) panchromatic camera; (b) multispectral color camera; (c) ASDs.

The primary cameras captured panchromatic and multispectral color images of three scenes, as shown in Figure 6. The red stars indicate the locations where ground personnel measured reflectance using ASDs, as shown in Figure 5c and detailed in Table 3.

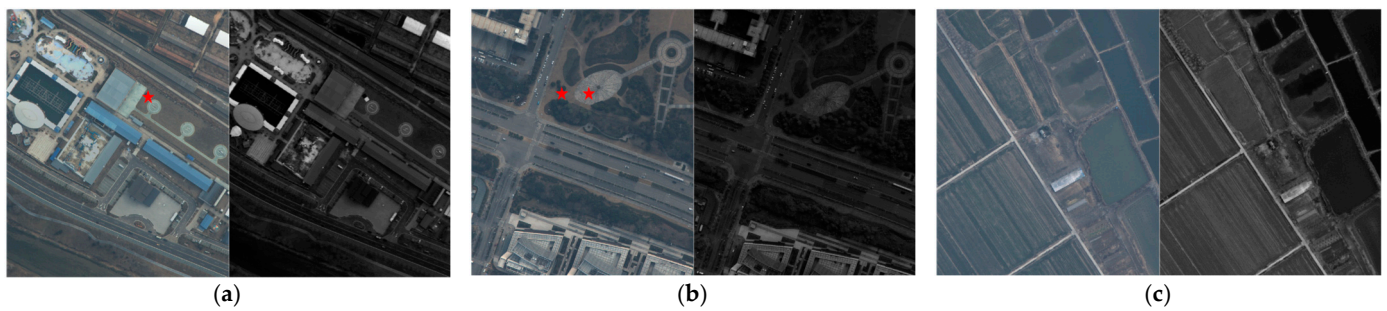


Figure 6. Panchromatic (right) and multispectral color (left) image: (a) artificial target scene; (b) road and grass scene; (c) cornfield scene.

Table 3. Surface reflectance measured by ASDs.

Type of Ground Object	Reflectivity Measured by the ASDs		
	R (570~690 nm)	G (450~660 nm)	B (380~570 nm)
Artificial white target	0.674	0.660	0.595
Artificial black target	0.041	0.042	0.043
Grass	0.166	0.135	0.097
Concrete floor	0.364	0.365	0.324

2.3.2. Atmospheric Parameter Images

Figure 7a,b provides physical diagrams of the VNIR-ASMAC and SWIR-ASMAC. The VNIR-ASMAC included three non-polarized bands (765, 910, and 950 nm) and three polarized bands (490, 670, and 870 nm). Similarly, the SWIR-ASMAC featured two non-polarized bands (950 and 1380 nm) and one polarized band (1610 nm). The multiangle, multiband polarimetric imaging capability of the ASMAC enabled the real-time monitoring of aerosol distribution in the atmosphere. The ASMAC underwent rigorous laboratory calibration, with each pixel subjected to geometric, radiometric, and polarization calibration, effectively treating each pixel as a radiance meter. Therefore, the remote sensing images captured by ASMAC can be inverted into AOD and CWV images [36].

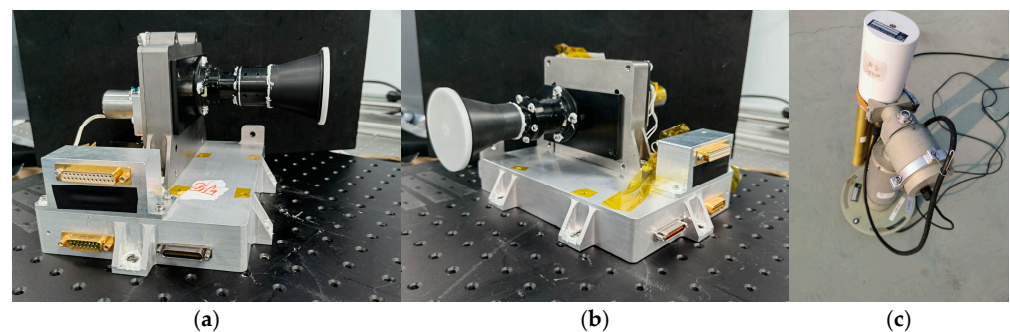


Figure 7. Atmospheric measurement instrument: (a) VNIR-ASMAC; (b) SWIR-ASMAC; (c) CE318.

Figure 8 illustrates the distribution images of AOD and CWV (already registered) corresponding to the remote sensing scenes, with their average and extremum values across the entire image plane listed in the Table 4. This indicates that each pixel in the panchromatic and multispectral images was associated with atmospheric parameters that are strictly synchronous in both time and space, thereby minimizing the impact of spatiotemporal heterogeneity in atmospheric parameters.

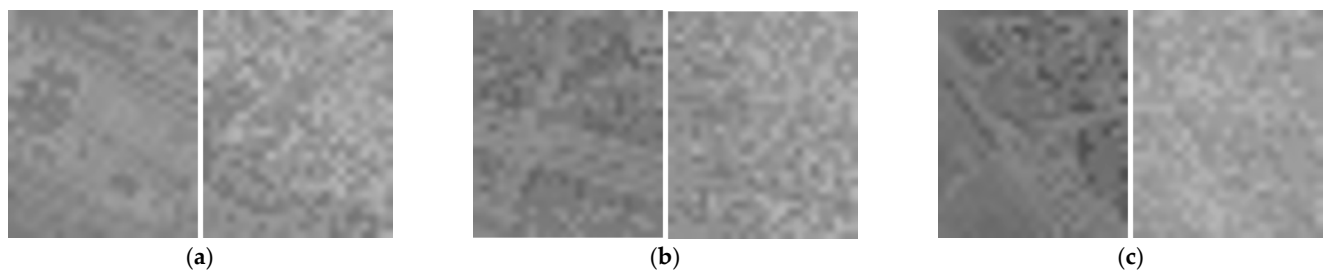


Figure 8. Synchronous AOD (left) and CWV (right) distribution images: (a) artificial target scene; (b) road and grass scene; (c) cornfield scene.

Table 4. The extremum and average values of the synchronous AOD and CWV images inverted from ASMAC.

Scene	AOD			CWV (g/cm ³)		
	Minimum	Average	Maximum	Minimum	Average	Maximum
Artificial target	0.441	0.549	0.626	0.976	1.273	1.539
Road and grass	0.384	0.494	0.587	0.981	1.226	1.493
Cornfield	0.465	0.501	0.593	1.121	1.317	1.554

Single-value atmospheric parameters representing asynchronous data were obtained from the CE318, as illustrated in Figure 7c. The single-value AOD and CWV were selected based on the acquisition time of the image, as shown in Table 5.

Table 5. The asynchronous single values of AOD and CWV measured from CE318.

Scene	AOD	CWV (g/cm ³)
Artificial target	0.548	1.436
Road and grass	0.552	1.442
Cornfield	0.545	1.445

2.4. Fusion Frameworks

The atmospheric parameter distribution images were used as source images and fused with panchromatic and multispectral remote sensing images. The fusion framework, as shown in Figure 9, was designed to explore various factors influencing the performance of the fused images. Four fusion experiments were conducted to investigate the effects of different fusion methods, atmospheric correction, the synchronization of atmospheric parameters, and the timing of atmospheric correction:

- Fusion 1: Disconnect all switches and perform decomposition or transformation only on the panchromatic and color remote sensing images. Then, select the fusion coefficients based on the fusion rules and reconstruct the fused image.
- Fusion 2: Connect the switch for Fusion 2, while keeping others disconnected. Single-value atmospheric parameter LUTs are used to perform atmospheric correction on the panchromatic and color remote sensing images, followed by decomposition or transformation. Then, select the fusion coefficients based on the fusion rules and reconstruct the fused image.
- Fusion 3: Connect the switch for Fusion 3, while keeping others disconnected. Synchronous atmospheric parameter distribution LUTs are used to apply imaging-based synchronous atmospheric correction to the panchromatic and color remote sensing images, followed by decomposition or transformation. Then, select the fusion coefficients based on the fusion rules and reconstruct the fused image.
- Fusion 4: Connect the switch for Fusion 4, while keeping others disconnected. Perform decomposition or transformation only on the panchromatic and color remote sensing

images. Then, select the fusion coefficients based on the fusion rules and reconstruct the fused image. Finally, an imaging-based synchronous atmospheric correction is applied to the fused image.

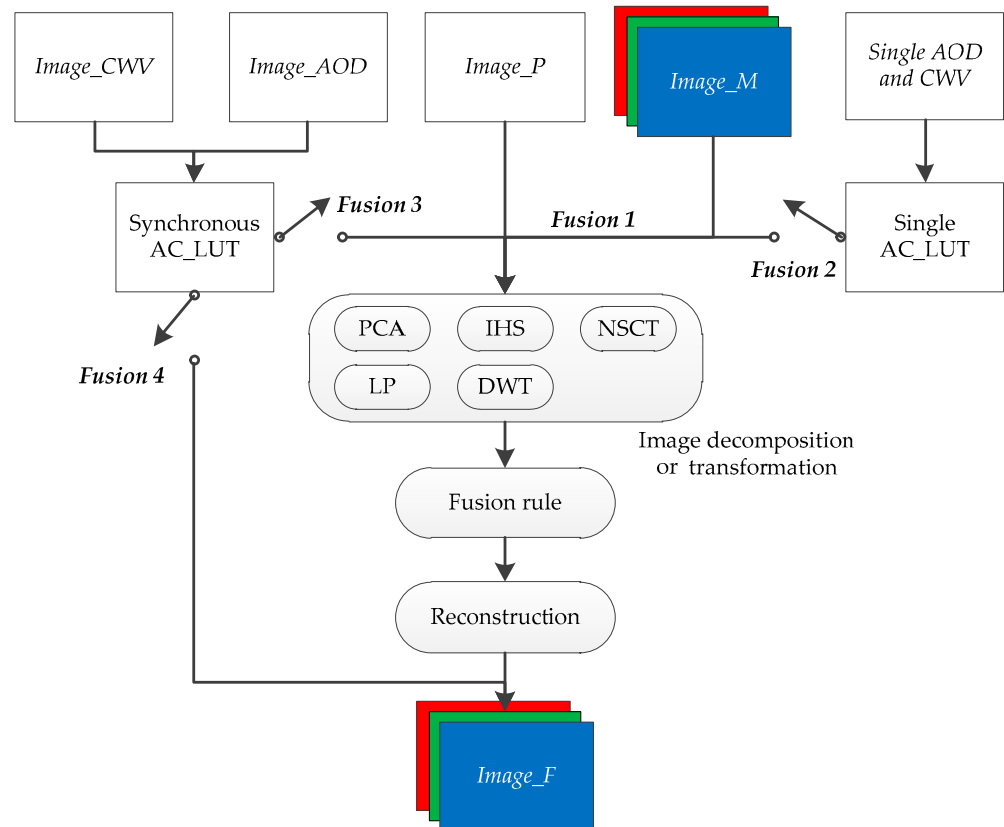


Figure 9. Experimental diagram of the interaction between atmospheric correction and fusion techniques.

Fusion 1 was derived solely from panchromatic and color remote sensing images. The evaluation results of this fused image can be used to assess the impact of different decomposition or transformation methods on the fusion outcome. The key difference between Fusion 1 and Fusion 2 was the inclusion of atmospheric parameters in the image sources. The evaluation results of these fused images can be used to compare the effect of atmospheric correction on the fusion outcome. The distinction between Fusion 2 and Fusion 3 lies in whether the atmospheric parameter distribution image was temporally and spatially synchronous with the panchromatic and color remote sensing images. These results can be used to analyze the effect of atmospheric parameter synchronization on the fusion outcome. Finally, the difference between Fusion 3 and Fusion 4 was the timing of the inclusion of atmospheric parameter distribution images in the fusion process. The evaluation results of these fused images can be used to compare the impact of atmospheric correction timing on fusion performance.

3. Results

3.1. Fused Image

Using the fusion methods and rules provided in Section 2.1, and following the fusion framework described in Section 2.4, panchromatic images, multispectral color images, and atmospheric parameter images from the three scenes described in Section 2.3 were fused. The resulting fused images are presented in Figures 10–13. The figures, from left to right, are the fused images obtained using the PCA, IHS, DWT, NSCT, and LP fusion methods,

respectively. Panels a–e depict the artificial target scene, f–j represent the road and grass scene, and k–o illustrate the wheat field scene.

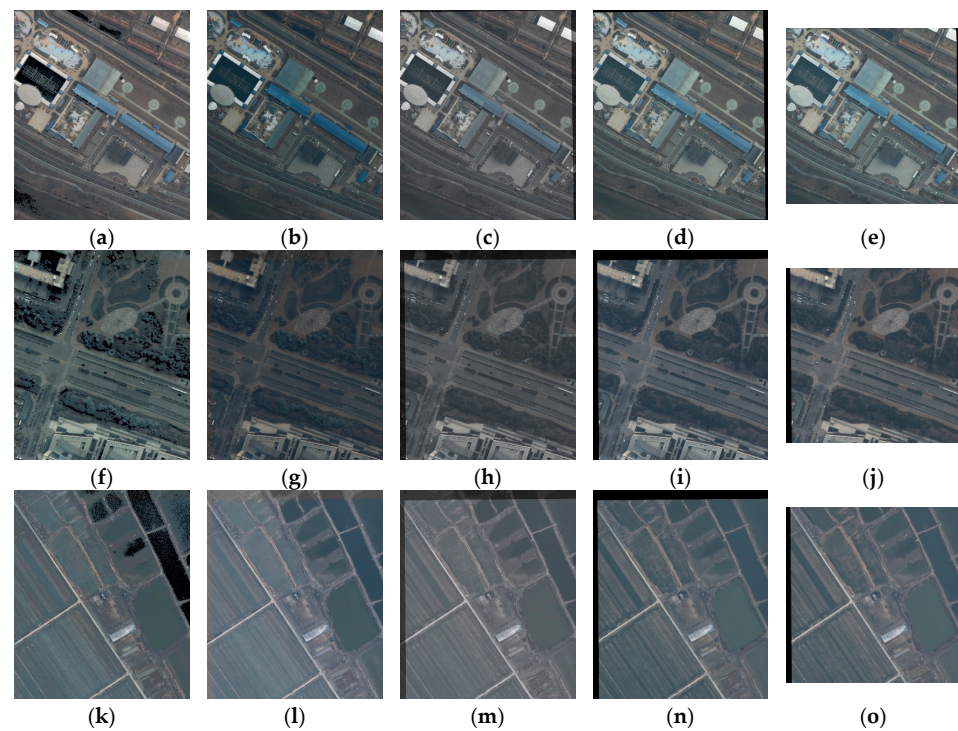


Figure 10. The fused images under Fusion 1. Each row, from left to right, is a fusion image of PCA, IHS, DWT, NSCT, and LP. (a–e) depict the artificial target scene, (f–j) represent the road and grass scene, and (k–o) illustrate the wheat field scene.

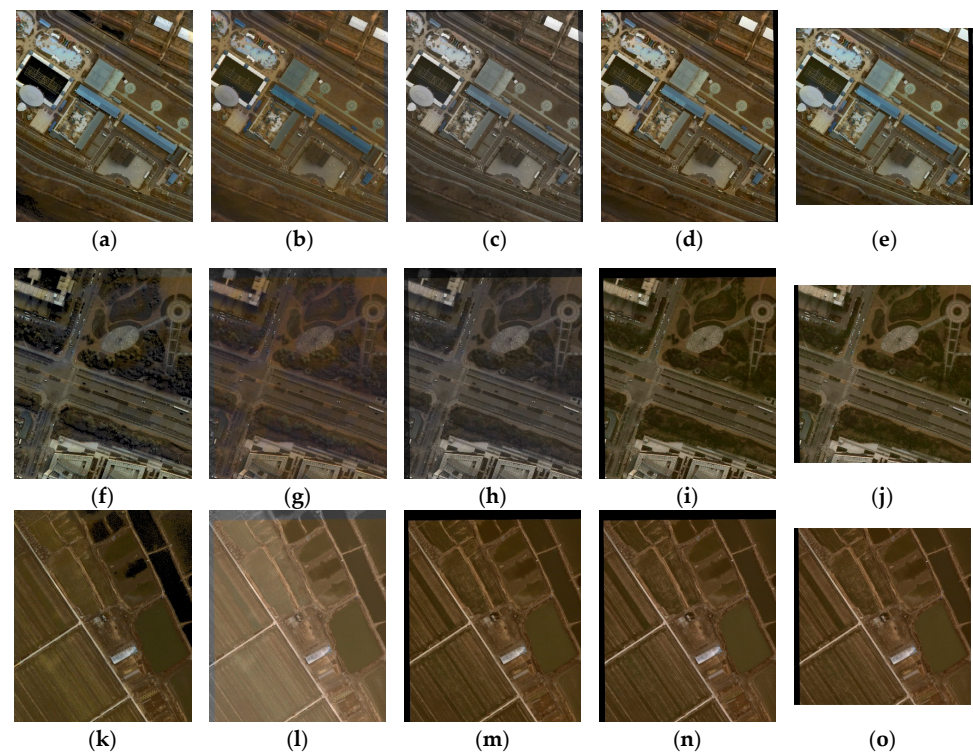


Figure 11. The fused images under Fusion 2. Each row, from left to right, is a fusion image of PCA, IHS, DWT, NSCT, and LP. (a–e) depict the artificial target scene, (f–j) represent the road and grass scene, and (k–o) illustrate the wheat field scene.

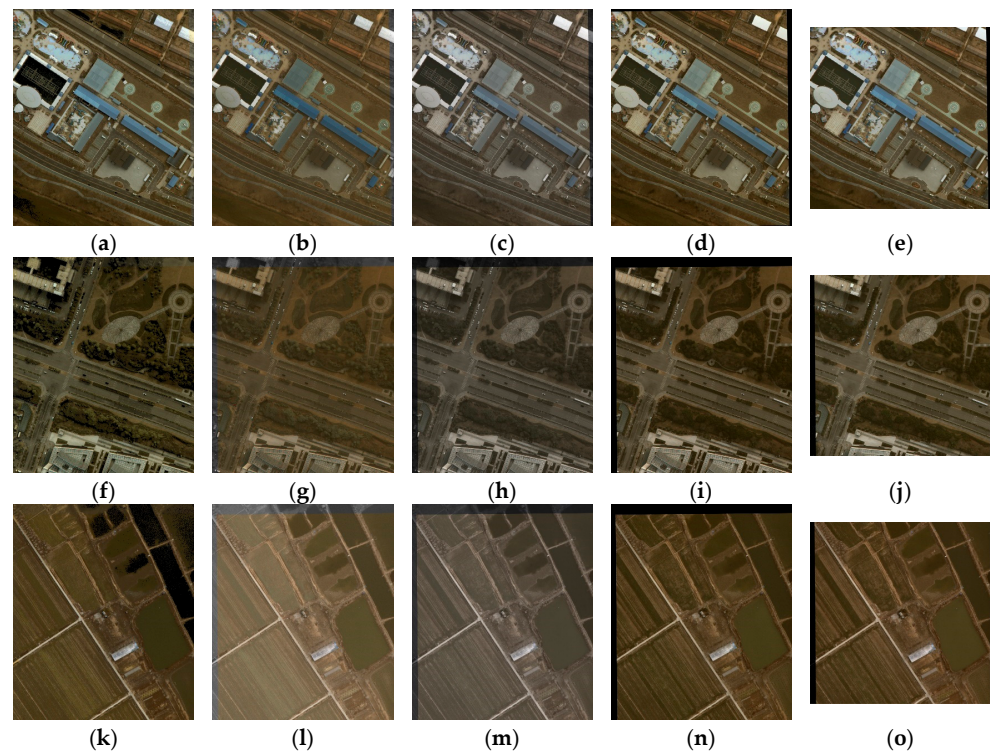


Figure 12. The fused images under Fusion 3. Each row, from left to right, is a fusion image of PCA, IHS, DWT, NSCT, and LP. (a–e) depict the artificial target scene, (f–j) represent the road and grass scene, and (k–o) illustrate the wheat field scene.

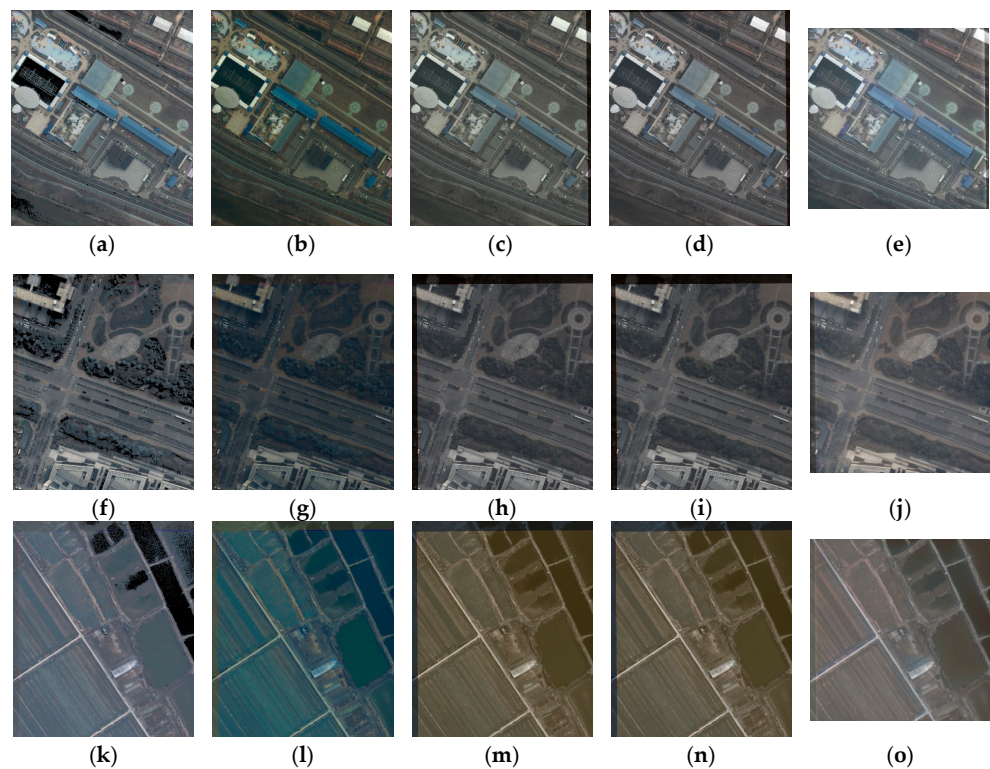


Figure 13. The fused images under Fusion 4. Each row, from left to right, is a fusion image of PCA, IHS, DWT, NSCT, and LP. (a–e) depict the artificial target scene, (f–j) represent the road and grass scene, and (k–o) illustrate the wheat field scene.

3.2. Spatial Detail Evaluation

This section provides an objective analysis of the fused images and evaluates them using the metrics described in Section 2.2.

3.2.1. Effects of Fusion Methods on Spatial Detail

Table 6 presents the evaluation values of UIQI, NCC, NMI, SSIM, and AG for the fused images obtained through five different fusion methods under Fusion 1. This was performed to compare the impact of the choice of fusion method on the spatial details of the fused images. The evaluation values represent the mean values across the RGB channels. Additionally, the extreme value ratio for each metric was calculated, indicating the ratio of the maximum to minimum evaluation values obtained through the different fusion methods.

Table 6. Evaluation metrics for fused images within the Fusion 1 framework.

Scene	Method	UIQI	NCC	NMI	SSIM	AG	SD	EN
Artificial target	PCA	0.486 *	0.941	0.749	0.323	2.36×10^{-3}	0.028	4.408
	IHS	0.832	0.925	0.740	0.628	3.11×10^{-3}	0.065	5.229
	DWT	0.847	0.946	0.755	0.793	4.30×10^{-3}	0.070	5.538
	NSCT	0.868	0.949	0.764	0.797	5.18×10^{-3}	0.073	5.731
	LP	0.834	0.826	0.716	0.763	3.76×10^{-3}	0.077	5.403
Extreme value ratio		1.786	1.149	1.068	2.471	2.192	2.739	1.300
Road and grass	PCA	0.485	0.791	0.709	0.310	2.61×10^{-3}	0.024	4.051
	IHS	0.839	0.853	0.701	0.639	2.96×10^{-3}	0.043	5.173
	DWT	0.850	0.922	0.728	0.803	3.55×10^{-3}	0.042	5.553
	NSCT	0.853	0.927	0.738	0.806	3.85×10^{-3}	0.044	5.747
	LP	0.836	0.804	0.699	0.580	2.81×10^{-3}	0.041	5.035
Extreme value ratio		1.760	1.171	1.056	2.597	1.475	1.827	1.419
Cornfield	PCA	0.467	0.720	0.662	0.339	1.85×10^{-3}	0.017	3.151
	IHS	0.808	0.758	0.652	0.640	2.02×10^{-3}	0.020	4.594
	DWT	0.812	0.878	0.687	0.703	1.89×10^{-3}	0.019	4.020
	NSCT	0.822	0.881	0.689	0.715	2.10×10^{-3}	0.019	3.999
	LP	0.807	0.837	0.673	0.709	2.06×10^{-3}	0.017	4.592
Extreme value ratio		1.759	1.223	1.057	2.111	1.135	1.191	1.458

* The maximum (optimal) and minimum (worst) evaluation values are highlighted using bold and italicized font in this table.

3.2.2. Effects of Atmospheric Correction and Parameter Synchronization on Spatial Detail

Table 7 presents the evaluation values of AG, SD, and EN for the fused images obtained through five different fusion methods under Fusion 1, Fusion 2, and Fusion 3. Since the source images in Fusion 1, Fusion 2, and Fusion 3 differ, using source-based evaluation metrics like UIQI, NCC, NMI, and SSIM are not meaningful. Instead, AG, SD, and EN, which are based on the statistical features of the fused images themselves, are employed, making them more comparable. Fusion 2 and Fusion 3 are utilized to assess the impact of atmospheric parameter synchronization on the spatial details of the fused images, while Fusion 1 and Fusion 3 are used to compare the effects of atmospheric correction on these details.

Table 7. Evaluation metrics for fused images within the Fusion 1, Fusion 2, and Fusion 3 framework.

Method	Framework	Artificial Target Scene			Road and Grass Scene			Cornfield Scene		
		AG	SD	EN	AG	SD	EN	AG	SD	EN
PCA	Fusion 1	2.36×10^{-3}	0.028	4.408	2.61×10^{-3}	0.024	4.051	1.85×10^{-3}	0.017	3.151
	Fusion 2	2.93×10^{-3}	0.039 *	4.950	2.90×10^{-3}	0.029	4.533	2.45×10^{-3}	0.020	3.569
	Fusion 3	2.94×10^{-3}	0.038	4.947	2.94×10^{-3}	0.030	4.477	2.53×10^{-3}	0.020	3.584
Extreme value ratio		1.25	1.38	1.12	1.13	1.25	1.12	1.369	1.168	1.137
IHS	Fusion 1	3.11×10^{-3}	0.065	5.229	2.96×10^{-3}	0.043	5.173	2.02×10^{-3}	0.020	4.594
	Fusion 2	6.07×10^{-3}	0.077	5.694	3.66×10^{-3}	0.051	5.434	2.58×10^{-3}	0.025	4.871
	Fusion 3	6.17×10^{-3}	0.078	5.607	3.88×10^{-3}	0.052	5.473	2.79×10^{-3}	0.025	4.917
Extreme value ratio		1.98	1.20	1.09	1.31	1.21	1.06	1.380	1.249	1.070
DWT	Fusion 1	4.30×10^{-3}	0.070	5.538	3.55×10^{-3}	0.042	5.553	1.89×10^{-3}	0.019	4.020
	Fusion 2	8.07×10^{-3}	0.082	5.780	4.10×10^{-3}	0.050	5.681	2.30×10^{-3}	0.023	4.313
	Fusion 3	8.12×10^{-3}	0.084	5.785	4.12×10^{-3}	0.051	5.727	2.43×10^{-3}	0.024	4.389
Extreme value ratio		1.89	1.19	1.04	1.16	1.21	1.03	1.281	1.295	1.092
NSCT	Fusion 1	5.18×10^{-3}	0.073	5.731	3.85×10^{-3}	0.044	5.747	2.10×10^{-3}	0.019	3.999
	Fusion 2	8.93×10^{-3}	0.084	6.074	3.97×10^{-3}	0.054	5.876	2.39×10^{-3}	0.023	4.292
	Fusion 3	8.97×10^{-3}	0.084	6.078	4.10×10^{-3}	0.054	5.882	2.51×10^{-3}	0.025	4.364
Extreme value ratio		1.73	1.15	1.06	1.07	1.23	1.02	1.195	1.348	1.091
LP	Fusion 1	3.76×10^{-3}	0.077	5.403	2.81×10^{-3}	0.041	5.035	2.06×10^{-3}	0.017	4.592
	Fusion 2	7.58×10^{-3}	0.093	6.157	3.38×10^{-3}	0.049	5.334	2.48×10^{-3}	0.024	4.891
	Fusion 3	7.64×10^{-3}	0.094	6.164	3.53×10^{-3}	0.049	5.351	2.63×10^{-3}	0.024	4.919
Extreme value ratio		2.03	1.23	1.14	1.26	1.22	1.06	1.276	1.394	1.071

* The maximum evaluation values (optimal value) are highlighted using bold and italicized font in this table.

3.2.3. Effects of Atmospheric Correction Timing on Spatial Detail

Similar to Table 7, Table 8 presents the evaluation values of AG, SD, and EN for the fused images obtained through five different fusion methods under Fusion 3 and Fusion 4. These metrics are utilized to compare the impact of the timing of atmospheric correction on the spatial details of the fused images.

Table 8. Evaluation metrics for fused images within the Fusion 3 and Fusion 4 framework.

Method	Framework	Artificial Target Scene			Road and Grass Scene			Cornfield Scene		
		AG	SD	EN	AG	SD	EN	AG	SD	EN
PCA	Fusion 3	2.94×10^{-3}	0.038	4.947	2.94×10^{-3}	0.030	4.477	2.53×10^{-3}	0.020	3.584
	Fusion 4	2.02×10^{-3}	0.024	4.418	2.28×10^{-3}	0.022	3.982	2.38×10^{-3}	0.015	3.344
Extreme value ratio		1.454	1.618	1.120	1.287	1.384	1.124	1.066	1.315	1.072
IHS	Fusion 3	6.17×10^{-3}	0.078	5.607	3.88×10^{-3}	0.052	5.473	2.79×10^{-3}	0.025	4.917
	Fusion 4	5.93×10^{-3}	0.063	5.012	3.55×10^{-3}	0.048	5.332	2.52×10^{-3}	0.023	4.858
Extreme value ratio		1.041	1.235	1.119	1.093	1.086	1.026	1.106	1.098	1.012
DWT	Fusion 3	8.12×10^{-3}	0.084	5.785	4.12×10^{-3}	0.051	5.727	2.43×10^{-3}	0.024	4.389
	Fusion 4	3.91×10^{-3}	0.059	5.601	3.03×10^{-3}	0.039	5.039	2.28×10^{-3}	0.023	4.296
Extreme value ratio		2.076	1.410	1.033	1.360	1.316	1.137	1.065	1.062	1.022
NSCT	Fusion 3	8.97×10^{-3}	0.084	6.078	4.10×10^{-3}	0.054	5.882	2.51×10^{-3}	0.025	4.364
	Fusion 4	3.77×10^{-3}	0.059	5.594	2.91×10^{-3}	0.039	5.034	2.17×10^{-3}	0.023	4.275
Extreme value ratio		2.376	1.410	1.086	1.407	1.399	1.168	1.156	1.106	1.021
LP	Fusion 3	7.64×10^{-3}	0.094	6.164	3.53×10^{-3}	0.049	5.351	2.63×10^{-3}	0.024	4.919
	Fusion 4	4.23×10^{-3}	0.085	6.038	3.21×10^{-3}	0.045	5.225	2.40×10^{-3}	0.021	4.793
Extreme value ratio		1.805	1.099	1.021	1.099	1.100	1.024	1.093	1.145	1.026

3.3. Spectral Quantification Evaluation

3.3.1. Effects of Fusion Methods on Spectral Quantification

Table 9 presents the DTR for the fusion images of the artificial targets and the roads and grassland scenes using five different fusion methods under Fusion 1. These values are used to assess the impact of the fusion methods on the spectral quantification of the fused image. DTR is expressed as a percentage, where smaller values indicate a closer approximation to the true reflectance. Similarly, the extreme values of DTR were also calculated.

Table 9. DTR for Fusion 1 framework.

Ground Type	Method	Calculated Reflectance			DTR		
		B	G	R	B	G	R
Black target	PCA	0.017	0.023	0.024	59.35%	45.29%	40.36%
	IHS	0.113	0.135	0.156	161.67%	221.19%	280.53%
	DWT	0.104	0.116	0.120	140.83%	175.20% *	193.60%
	NSCT	0.102	0.111	0.114	138.08%	163.66%	178.17%
	LP	0.103	0.123	0.125	139.45%	193.26%	204.85%
White target	PCA	0.089	0.164	0.254	85.06%	75.14%	62.25%
	IHS	0.468	0.538	0.622	21.34%	18.52%	7.76%
	DWT	0.377	0.397	0.411	36.70%	39.86%	39.02%
	NSCT	0.375	0.412	0.421	36.92%	37.59%	37.54%
	LP	0.352	0.394	0.423	40.77%	40.29%	37.28%
Concrete floor	PCA	0.074	0.144	0.213	77.19%	60.47%	41.60%
	IHS	0.266	0.339	0.410	17.88%	7.16%	12.64%
	DWT	0.205	0.237	0.233	36.87%	35.02%	36.10%
	NSCT	0.210	0.237	0.229	35.28%	35.18%	36.97%
	LP	0.203	0.212	0.228	37.35%	41.92%	37.36%
Grass	PCA	0.042	0.078	0.123	56.95%	42.35%	25.86%
	IHS	0.154	0.191	0.236	59.08%	41.25%	42.34%
	DWT	0.147	0.175	0.229	51.94%	29.60%	37.69%
	NSCT	0.149	0.170	0.224	54.10%	26.28%	34.81%
	LP	0.163	0.180	0.241	68.41%	33.64%	45.00%

* When considering the evaluation metrics for DWT, NSCT, and LP fused images, the maximum and minimum values are highlighted in bold and italicized font in this table.

3.3.2. Effects of Atmospheric Correction and Parameter Synchronization on Spectral Quantification

Due to the inconsistent performance of IHS and PCA in improving spectral quantification (as discussed in Section 4.1), only transform-domain-based fusion methods are considered in the discussion. Table 10 presents the DTR values for the fused images of artificial targets, roads, and grassland scenes, obtained using three transform-domain-based fusion methods within Fusion 1, Fusion 2, and Fusion 3. These values are used to evaluate the impact of atmospheric parameters and their synchronization on the spectral quantification of the fused images.

Table 10. DTR for the Fusion 1, Fusion 2, and Fusion 3 framework.

Ground Type	Method and DTR	B			G			R		
		Fusion 1	Fusion 2	Fusion 3	Fusion 1	Fusion 2	Fusion 3	Fusion 1	Fusion 2	Fusion 3
Black target	DWT	0.104	0.056	0.051	0.116	0.052	0.049	0.120	0.061	0.051
	NSCT	0.102	0.053	0.048	0.111	0.049	0.046	0.114	0.057	0.047
	LP	0.103	0.058	0.053	0.123	0.060	0.057	0.125	0.071	0.061
	DTR _{DWT}	140.8%	30.5%	18.9%	175.2%	23.1%	16.3%	193.6%	48.4%	23.7%
	DTR _{NSCT}	138.1%	23.2%	11.6%	163.7%	16.2%	9.4%	178.2%	39.9%	15.2%
	DTR _{LP}	139.5%	34.6%	22.9%	193.3%	42.0%	35.3%	204.8%	72.2%	47.6%

Table 10. Cont.

Ground Type	Method and DTR	B			G			R		
		Fusion 1	Fusion 2	Fusion 3	Fusion 1	Fusion 2	Fusion 3	Fusion 1	Fusion 2	Fusion 3
White target	DWT	0.377	0.545	0.557	0.397	0.542	0.494	0.411	0.516	0.611
	NSCT	0.375	0.532	0.544	0.412	0.547	0.499	0.421	0.506	0.602
	LP	0.352	0.516	0.529	0.394	0.529	0.481	0.423	0.515	0.610
	DTR _{DWT}	36.7%	8.5%	6.3%	39.9%	17.8%	25.2%	39.0%	23.5%	9.4%
	DTR _{NSCT}	36.9%	10.6%	8.5%	37.6%	17.1%	24.4%	37.5%	24.9%	10.7%
	DTR _{LP}	40.8%	13.2%	11.1%	40.3%	19.8%	27.2%	37.3%	23.6%	9.5%
Concrete floor	DWT	0.205	0.261	0.282	0.237	0.293	0.329	0.233	0.313	0.314
	NSCT	0.210	0.252	0.273	0.237	0.285	0.320	0.229	0.320	0.321
	LP	0.203	0.255	0.276	0.212	0.261	0.297	0.228	0.315	0.316
	DTR _{DWT}	36.9%	19.6%	13.1%	35.0%	19.7%	10.0%	36.1%	14.0%	13.8%
	DTR _{NSCT}	35.3%	22.2%	15.8%	35.2%	21.9%	12.3%	37.0%	12.1%	11.9%
	DTR _{LP}	37.4%	21.3%	14.8%	41.9%	28.4%	18.7%	37.4%	13.4%	13.2%
Grass	DWT	0.147	0.102	0.106	0.175	0.149	0.154	0.229	0.185	0.181
	NSCT	0.149	0.104	0.108	0.170	0.142	0.146	0.224	0.179	0.176
	LP	0.163	0.118	0.122	0.180	0.151	0.156	0.241	0.195	0.192
	DTR _{DWT}	51.9%	5.4%	9.5%	29.6%	10.7%	14.1%	37.7%	11.2%	9.1%
	DTR _{NSCT}	54.1%	6.9%	11.1%	26.3%	5.0%	8.4%	34.8%	7.9%	5.8%
	DTR _{LP}	68.4%	21.9%	26.1%	33.6%	12.0%	15.4%	45.0%	17.5%	15.4%

3.3.3. Effects of Atmospheric Correction Timing on Spectral Quantification

Similar to Table 10, Table 11 presents the DTR values for the fused images of artificial targets, roads, and grassland scenes, obtained using three transform-domain-based fusion methods within Fusion 3 and Fusion 4. These values are used to evaluate the impact of the timing of atmospheric correction on the spectral quantification of the fused images.

Table 11. DTR for the Fusion 3 and Fusion 4 framework.

Ground Type	Method and DTR	B		G		R	
		Fusion 3	Fusion 4	Fusion 3	Fusion 4	Fusion 3	Fusion 4
Black target	DWT	0.051	0.054	0.049	0.049	0.051	0.053
	NSCT	0.048	0.050	0.046	0.048	0.047	0.052
	LP	0.053	0.054	0.057	0.061	0.061	0.066
	DTR _{DWT}	18.9%	25.4%	16.3%	17.6%	23.7%	28.4%
	DTR _{NSCT}	11.6%	16.1%	9.4%	13.7%	15.2%	25.6%
	DTR _{LP}	22.9%	26.7%	35.3%	46.1%	47.6%	60.8%
White target	DWT	0.557	0.510	0.494	0.451	0.611	0.599
	NSCT	0.544	0.530	0.499	0.471	0.602	0.589
	LP	0.529	0.520	0.481	0.466	0.610	0.563
	DTR _{DWT}	6.3%	14.2%	25.2%	31.7%	9.4%	11.1%
	DTR _{NSCT}	8.5%	10.9%	24.4%	28.7%	10.7%	12.6%
	DTR _{LP}	11.1%	12.5%	27.2%	29.5%	9.5%	16.4%
Concrete floor	DWT	0.282	0.281	0.329	0.319	0.314	0.307
	NSCT	0.273	0.268	0.320	0.309	0.321	0.317
	LP	0.276	0.271	0.297	0.292	0.316	0.312
	DTR _{DWT}	13.1%	13.3%	10.0%	12.5%	13.8%	15.6%
	DTR _{NSCT}	15.8%	17.3%	12.3%	15.2%	11.9%	12.9%
	DTR _{LP}	14.8%	16.2%	18.7%	20.1%	13.2%	14.3%
Grass	DWT	0.106	0.109	0.154	0.165	0.181	0.120
	NSCT	0.108	0.111	0.146	0.155	0.176	0.191
	LP	0.122	0.128	0.156	0.178	0.192	0.123
	DTR _{DWT}	9.5%	12.1%	14.1%	21.9%	9.1%	27.7%
	DTR _{NSCT}	11.1%	14.8%	8.4%	14.5%	5.8%	15.1%
	DTR _{LP}	26.1%	32.0%	15.4%	32.1%	15.4%	25.9%

4. Discussion

4.1. Effects of Fusion Methods

Table 6 presents the UIQI, NCC, NMI, SSIM, and AG values for fused images under Fusion 1. These metrics are used to compare the impact of different fusion methods on the spatial details of the fused images. The findings summarized from Table 6 are as follows:

1. In the three scenarios examined, the NSCT-based fusion method consistently demonstrates the best evaluation values. Generally, transform-domain-based fusion methods perform better than spatial-domain-based methods.
2. Among the three transform-domain-based fusion methods, NSCT outperforms DWT, and DWT performs better than LP.
3. The ratio of the extreme values indicates that, for the artificial target scene, selecting an appropriate fusion method can enhance the spatial details of the fused images by a factor of 1.149 to 2.739. For road and grassland scenes, the enhancement ranges from 1.056 to 2.597 times, while for the wheat field scene, the enhancement ranges from 1.057 to 2.111 times.

Spatial-domain fusion methods involve mathematical or statistical computations on pixels, which can result in a decreased contrast in the fused image and may not effectively preserve the detailed features of the original images. This is due to the less refined nature of image decomposition in the spatial domain, making it theoretically challenging to achieve satisfactory fusion results. In contrast, transform-domain fusion methods utilize multiscale decomposition techniques to represent images at various scales, resolutions, and orientations. This approach allows the fusion process to occur in the transform domain, offering a greater variety of optional fusion rules and finer control. These characteristics enable transform-domain fusion to preserve spatial information from the original images as much as possible. The enhancement of spatial details in fused images depends on the “fineness” of the image decomposition. Consequently, the NSCT method, which achieves a higher degree of image decomposition, demonstrates relatively superior fusion performance.

Table 9 presents the DTR values for fused images under the Fusion 1 framework, used to compare the impact of different fusion methods on the spectral quantification of the fused images. The results in Table 9 indicate that PCA-based fused images exhibit the smallest DTR for black targets, while IHS-based fused images show the smallest DTR for white targets and cement surfaces. Conversely, PCA-based fused images have the largest DTR for white targets, and IHS-based fused images demonstrate the largest DTR for black targets. This suggests that the DTR stability of PCA and IHS fusion methods is relatively poor. In contrast, the DTR stability for images fused using the DWT, NSCT, and LP methods is superior, making the evaluation of transform-domain fusion methods for spectral quantification more meaningful and practical. The summarized DTR results for transform-domain fusion methods from Table 9 are as follows:

1. For black targets, selecting an appropriate fusion method can reduce the DTR of the fused images from a maximum of 193.26% to 175.20% (G channel);
2. For white targets, selecting an appropriate fusion method can reduce the DTR from a maximum of 40.77% to 36.70% (B channel);
3. For cement surfaces, selecting an appropriate fusion method can reduce the DTR from a maximum of 41.92% to 35.02% (G channel);
4. For the grassland, selecting an appropriate fusion method can reduce the DTR from a maximum of 68.41% to 51.97% (B channel).

Due to the complexity of image edges and texture information, which involve various land cover components, spectral quantification is often compared using flat, homogeneous land targets. In such cases, the spectral quantification of fused images primarily depends on the low-frequency signals. Transform domain fusion methods effectively separate low-frequency and high-frequency signals in a stable and detailed manner, resulting in better DTR stability for images fused using the DWT, NSCT, and LP methods.

4.2. Effects of Atmospheric Correction and Synchronous of Parameters

Table 7 presents the AG, SD, and EN values for fused images under Fusion 1, Fusion 2, and Fusion 3, which are used to compare the impact of atmospheric parameters and their synchronization on the spatial details of the fused images. The findings summarized from Table 7 are as follows:

1. The evaluation values for Fusion 1 are the lowest among all fusion methods, indicating that introducing atmospheric parameters into the fusion process can effectively enhance the spatial details of the fused images.
2. The highest evaluation values for most fusion methods are observed in Fusion 3, while PCA and IHS fusion images show a few highest values in Fusion 2. This indicates that synchronous atmospheric parameters have the greatest impact on improving the spatial details of the fused images.
3. The ratio of the extreme values indicates that, for the artificial target scene, the synchronous atmospheric parameter can enhance the spatial details of the fused images by 1.04 to 2.03 times. For road and grassland scenes, the enhancement ranges from 1.02 to 1.31 times. For the wheat field scene, the enhancement ranges from 1.070 to 1.380 times.

Atmospheric effects can cause blurring in remote sensing images, leading to unclear spatial details and textures. By incorporating atmospheric parameters into the fusion process, these effects can be mitigated, and the contrast of the fused images can be improved. Synchronous atmospheric parameter maps are particularly effective in addressing the spatiotemporal heterogeneity of aerosols, resulting in a more significant enhancement of spatial details.

Table 10 presents the DTR values for fused images under Fusion 1, Fusion 2, and Fusion 3, which are used to compare the impact of atmospheric parameters and their synchronization on the spectral quantification of the fused images. The results in Table 10 indicate that Fusion 1 exhibits the highest DTR values, while Fusion 3 shows the lowest DTR values for most cases. Fusion 2 has the lowest DTR values for a few grassland scenarios. The summarized results from Table 10 are as follows:

1. For black targets, synchronous atmospheric parameters can reduce the DTR of the fused images from a maximum of 163.7% to 9.4% (G channel);
2. For white targets, synchronous atmospheric parameters can reduce the DTR from a maximum of 36.7% to 6.3% (B channel);
3. For cement surfaces, synchronous atmospheric parameters can reduce the DTR from a maximum of 35.0% to 10.0% (G channel);
4. For the grassland, atmospheric parameters can reduce the DTR of the fused images from a maximum of 51.9% to 5.4% (B channel).

Atmospheric effects are one of the primary factors causing spectral distortion in remote sensing images. Fusion processes can introduce these distorted signals into the fused images, and strict fusion rules alone cannot eliminate atmospheric information. By incorporating atmospheric parameters as sources in the fusion process, these effects can be effectively mitigated or even eliminated. Synchronous atmospheric parameter maps further address the spatiotemporal heterogeneity of aerosols, leading to enhanced spectral quantification in the fused images.

4.3. Effects of the Timing of Atmospheric Correction

Table 8 presents the AG, SD, and EN values for fused images under Fusion 3 and Fusion 4, which are used to compare the impact of the timing of atmospheric correction on the spatial details of the fused images. The results in Table 8 indicate that Fusion 4 consistently shows lower evaluation values than Fusion 3 across all fusion methods, suggesting that performing atmospheric correction before image fusion leads to a greater enhancement of spatial details in the fused images.

Table 11 presents the DTR values for fused images under Fusion 3 and Fusion 4, which are used to compare the impact of the timing of atmospheric correction on the spectral quantification of the fused images. The results in Table 11 indicate that the DTR values for all land cover targets computed in Fusion 3 are lower than those in Fusion 4, suggesting that performing atmospheric correction prior to image fusion leads to a greater improvement in the spectral quantification of the fused images.

5. Conclusions

This study investigates the impact of 6S atmospheric correction combined with five image fusion methods (PCA, IHS, DWT, LP, and NSCT) on the performance of fused images, focusing on four aspects: the choice of fusion method, the implementation of atmospheric correction, the synchronization of atmospheric parameters, and the timing of atmospheric correction.

The experimental results for each fusion method indicate that the choice of fusion technique significantly affects the spatial details of remote sensing fused images. In three experimental scenarios, selecting an appropriate fusion method can enhance the spatial detail evaluation values of the fused images by factors of 1.149 to 2.739, 1.056 to 2.597, and 1.057 to 2.111, respectively. However, the choice of fusion method has a relatively minor impact on the spectral quantification of remote sensing images. The maximum reduction in DTR for black targets, white targets, cement surfaces, and the grassland was observed to be as follows: from 193.26% to 175.20%, from 40.77% to 36.70%, from 41.92% to 35.02%, and from 68.41% to 51.97%, respectively.

Experiments employing different atmospheric parameters for atmospheric correction demonstrate that atmospheric correction improves the performance of fused images across all methods, with synchronized atmospheric parameter maps yielding better results than single-value atmospheric parameters. In the three experimental scenarios, atmospheric correction enhances the spatial details of PCA, IHS, DWT, NSCT, and LP fused images by factors ranging from 1.12 to 1.38, 1.06 to 1.98, 1.03 to 1.89, 1.02 to 1.73, and 1.06 to 2.03, respectively. Additionally, atmospheric correction reduces the DTR for four types of features (black targets, white targets, cement surfaces, and grassland), with maximum reductions of the following: from 163.7% to 9.4%, from 36.7% to 6.3%, from 35.0% to 10.0%, and from 51.9% to 5.4%. Furthermore, experiments conducted at different timings for atmospheric correction indicate that placing the atmospheric correction step before the fusion step yields better results.

In summary, integrating synchronized atmospheric parameter distribution images into the fusion framework prior to remote sensing image fusion, along with selecting fusion methods based on multiscale decomposition, such as NSCT, can significantly enhance both the spatial details and spectral quantification of fused images. The findings of this study provide a technical pathway for achieving the high-quality quantitative fusion of remote sensing images.

While this research demonstrates the impact of 6S atmospheric correction and five fusion techniques on the performance of fused images, future work will explore deep-learning-based methods. Deep learning approaches not only hold promise for image fusion but may also address challenges related to atmospheric correction and aerosol parameter inversion, necessitating further investigation.

Author Contributions: Conceptualization, Z.Q.; methodology, Y.L.; validation, F.C., T.S. and Y.L.; formal analysis, Y.L.; investigation, Y.L., F.C., T.S., W.C. and R.T.; resources, Y.L.; data curation, Y.L.; writing—original draft preparation, Y.L.; writing—review and editing, Y.L.; visualization, Y.L.; supervision, Y.L.; project administration, Z.Q. and J.H.; funding acquisition, Z.Q. All authors have read and agreed to the published version of the manuscript.

Funding: This research was funded by the Chinese Civil Aerospace Program, grant number D010206.

Data Availability Statement: The dataset is available on request from the authors.

Acknowledgments: Yang Li is very grateful to Rufang Ti for her help on the aerosol retrieval algorithm and Tangyu Sui for his help on the atmospheric correction.

Conflicts of Interest: The authors declare no conflicts of interest.

References

- Li, Y.; Qiu, Z.; Chen, F.; Sui, T.; Ti, R.; Cheng, W.; Hong, J. Remote sensing image registration method based on synchronous atmospheric correction. *Opt. Express* **2024**, *32*, 24573–24591. [[CrossRef](#)]
- Zhang, H.; Ma, J. SDNet: A Versatile Squeeze-and-Decomposition Network for Real-Time Image Fusion. *Int. J. Comput. Vis.* **2021**, *129*, 2761–2785. [[CrossRef](#)]
- Singh, S.; Singh, H.; Bueno, G.; Deniz, O.; Singh, S.; Monga, H.; Hrisheekesha, P.N.; Pedraza, A. A review of image fusion: Methods, applications and performance metrics. *Digit. Signal Process.* **2023**, *137*, 104020. [[CrossRef](#)]
- Chughtai, A.H.; Abbasi, H.; Ismail, R.K. A review on change detection method and accuracy assessment for land use land cover. *Remote Sens. Appl. Soc. Environ.* **2021**, *22*, 100482. [[CrossRef](#)]
- Yang, Y.; Anderson, M.C.; Gao, F.; Wood, J.D.; Gu, L.; Hain, C. Studying drought-induced forest mortality using high spatiotemporal resolution evapotranspiration data from thermal satellite imaging. *Remote Sens. Environ.* **2021**, *265*, 112640. [[CrossRef](#)]
- Nguyen, T.-A.; Kellenberger, B.; Tuia, D. Mapping forest in the Swiss Alps treeline ecotone with explainable deep learning. *Remote Sens. Environ.* **2022**, *281*, 113217. [[CrossRef](#)]
- Kavitha, A.V.; Srikrishna, A.; Satyanarayana, C. Crop image classification using spherical contact distributions from remote sensing images. *J. King Saud Univ.-Comput. Inf. Sci.* **2022**, *34*, 534–545. [[CrossRef](#)]
- Al-Doski, J.; Hassan, F.M.; Norman, M.; Najim, A.A. Interaction of image fusion techniques and atmospheric correction for improve SVM accuracy. *Earth Sci. Inform.* **2022**, *15*, 2673–2687. [[CrossRef](#)]
- Kim, Y.; Lee, C.; Han, D.; Kim, Y.; Kim, Y. Improved Additive-Wavelet Image Fusion. *IEEE Geosci. Remote Sens. Lett.* **2011**, *8*, 263–267. [[CrossRef](#)]
- Yang, S.; Wang, M.; Jiao, L. Contourlet hidden Markov Tree and clarity-saliency driven PCNN based remote sensing images fusion. *Appl. Soft Comput.* **2012**, *12*, 228–237. [[CrossRef](#)]
- Fang, F.; Li, F.; Shen, C.; Zhang, G. A Variational Approach for Pan-Sharpener. *IEEE Trans. Image Process. A Publ. IEEE Signal Process. Soc.* **2013**, *22*, 2822–2834. [[CrossRef](#)] [[PubMed](#)]
- El-Mezouar, M.C.; Kpalma, K.; Taleb, N.; Ronsin, J. A Pan-Sharpener Based on the Non-Subsampled Contourlet Transform: Application to Worldview-2 Imagery. *IEEE J. Sel. Top. Appl. Earth Obs. Remote Sens.* **2014**, *7*, 1806–1815. [[CrossRef](#)]
- Shi, C.; Liu, F.; Miao, Q. Pan-sharpening via regional division and NSST. *Multimed. Tools Appl.* **2015**, *74*, 7843–7857. [[CrossRef](#)]
- Poobalabramanian, M.; Agrawal, A. Fusion of PAN and multispectral remote sensing images in shearlet domain by considering regional metrics. *J. Appl. Remote Sens.* **2016**, *10*, 045003. [[CrossRef](#)]
- Song, H.; Liu, Q.; Wang, G.; Hang, R.; Huang, B. Spatiotemporal Satellite Image Fusion Using Deep Convolutional Neural Networks. *IEEE J. Sel. Top. Appl. Earth Obs. Remote Sens.* **2018**, *11*, 821–829. [[CrossRef](#)]
- Ma, J.; Ma, Y.; Li, C. Infrared and visible image fusion methods and applications: A survey. *Inf. Fusion* **2019**, *45*, 153–178. [[CrossRef](#)]
- Singh, H.; Cristobal, G.; Blanco, S.; Bueno, G.; Sanchez, C. Nonsubsampled contourlet transform based tone mapping operator to optimize the dynamic range of diatom shells. *Microsc. Res. Tech.* **2021**, *84*, 2034–2045. [[CrossRef](#)]
- Tang, L.; Zhang, H.; Xu, H.; Ma, J. Deep learning-based image fusion: A survey. *J. Image Graph.* **2023**, *28*, 3–36. [[CrossRef](#)]
- Ma, J.; Yu, W.; Chen, C.; Liang, P.; Guo, X.; Jiang, J. Pan-GAN: An unsupervised pan-sharpening method for remote sensing image fusion. *Inf. Fusion* **2020**, *62*, 110–120. [[CrossRef](#)]
- Tang, L.; Yuan, J.; Ma, J. Image fusion in the loop of high-level vision tasks: A semantic-aware real-time infrared and visible image fusion network. *Inf. Fusion* **2022**, *82*, 28–42. [[CrossRef](#)]
- Liu, J.; Fan, X.; Jiang, J.; Liu, R.; Luo, Z. Learning a Deep Multi-Scale Feature Ensemble and an Edge-Attention Guidance for Image Fusion. *IEEE Trans. Circuits Syst. Video Technol.* **2022**, *32*, 105–119. [[CrossRef](#)]
- Yang, J.; Fu, X.; Hu, Y.; Huang, Y.; Ding, X.; Paisley, J. PanNet: A Deep Network Architecture for Pan-Sharpener. In Proceedings of the 2017 IEEE International Conference on Computer Vision (ICCV), Venice, Italy, 22–29 October 2017.
- Cai, J.; Huang, B. Super-Resolution-Guided Progressive Pansharpening Based on a Deep Convolutional Neural Network. *IEEE Trans. Geosci. Remote Sens.* **2020**, *59*, 1–15. [[CrossRef](#)]
- Xu, S.; Zhang, J.; Zhao, Z.; Sun, K.; Liu, J.; Zhang, C. Deep Gradient Projection Networks for Pan-Sharpener. In Proceedings of the IEEE/CVF Conference on Computer Vision and Pattern Recognition (CVPR), Nashville, TN, USA, 20–25 June 2021.
- Zhang, H.; Ma, J. GTP-PNet: A residual learning network based on gradient transformation prior for pansharpening. *ISPRS J. Photogramm. Remote Sens.* **2021**, *172*, 223–239. [[CrossRef](#)]
- Yin, F.; Gomez-Dans, J.; Lewis, P. A Sensor Invariant Atmospheric Correction Method for Satellite Images. In Proceedings of the IGARSS 2018-2018 IEEE International Geoscience and Remote Sensing Symposium, Valencia, Spain, 22–27 July 2018.
- Doxani, G.; Vermote, E.; Roger, J.C. Atmospheric Correction Inter-Comparison Exercise. *Remote Sens.* **2018**, *10*, 352. [[CrossRef](#)]
- Wang, T.; Zhou, N.; Yi, W. Adjacency effect correction of optical satellite image with sub-meter spatial resolution. *Acta Phys. Sin.* **2021**, *70*, 139101-1–139101-8. [[CrossRef](#)]

29. Ankarao, V.; Sowmya, V.; Soman, K.P. Multi-sensor data fusion using NIHS transform and decomposition algorithms. *Multimed. Tools Appl.* **2018**, *77*, 30381–30402. [[CrossRef](#)]
30. Shivsubramani, K.; Soman, K.P. Implementation and Comparative Study of Image Fusion Algorithms. *Int. J. Comput. Appl.* **2010**, *9*, 10–20.
31. Alseelawi, N.; Tuama Hazim, H.; Alrikabi, H.T.S. A Novel Method of Multimodal Medical Image Fusion Based on Hybrid Approach of NSCT and DTCWT. *Int. J. Online Biomed. Eng. (IJOE)* **2022**, *18*, 114–133. [[CrossRef](#)]
32. Ghassemian, H. A review of remote sensing image fusion methods. *Inf. Fusion* **2016**, *32*, 75–89. [[CrossRef](#)]
33. Zhang, P. Image Fusion Algorithm Based on Region Energy and Block Matching. Master's Thesis, Beijing Jiaotong University, Beijing, China, 2018.
34. Tanre, D.; Deuze, J.L.; Herman, M.; Morcette, J.J. Second Simulation of the Satellite Signal in the Solar Spectrum, 6S: An overview. *IEEE Trans. Geosci. Remote Sens.* **2002**, *35*, 675–686.
35. Wilson, T.R. Py6S: A Python interface to the 6S radiative transfer model. *Comput. Geosciences* **2013**, *51*, 166–171. [[CrossRef](#)]
36. Fan, Y.; Sun, X.; Ti, R.; Huang, H.; Liu, X.; Yu, H. Aerosol Retrieval Study from a Particulate Observing Scanning Polarimeter Onboard Gao-Fen 5B without Prior Surface Knowledge, Based on the Optimal Estimation Method. *Remote Sens.* **2023**, *15*, 385. [[CrossRef](#)]
37. Wang, W.; Chang, F. A Multi-focus Image Fusion Method Based on Laplacian Pyramid. *J. Comput.* **2011**, *6*, 2559–2566. [[CrossRef](#)]
38. Kulkarni, S.C.; Rege, P.P. Pixel level fusion techniques for SAR and optical images: A review. *Inf. Fusion* **2020**, *59*, 13–29. [[CrossRef](#)]
39. Wang, Z.; Bovik, A.C. A universal image quality index. *IEEE Signal Process. Lett.* **2002**, *9*, 81–84. [[CrossRef](#)]
40. Tsai, D.Y.; Lee, Y.; Matsuyama, E. Information entropy measure for evaluation of image quality. *J. Digit. Imaging* **2008**, *21*, 338–347. [[CrossRef](#)]

Disclaimer/Publisher's Note: The statements, opinions and data contained in all publications are solely those of the individual author(s) and contributor(s) and not of MDPI and/or the editor(s). MDPI and/or the editor(s) disclaim responsibility for any injury to people or property resulting from any ideas, methods, instructions or products referred to in the content.